408

Egypt. J. Chem. **Vol. 63,** No. 12 pp. 5161 - 5173 (2020)

Egyptian Journal of Chemistry

http://ejchem.journals.ekb.eg/

Desalination Performance of Thin-film Composite Forward Osmosis Membranes Based on Different Carbon Nanomaterials

Amira M. Shawky[a],*, Yousra H. Kotp[b], M.A. Mousa[c], Mostafa M. S. Aboelfadl[b], E. E. Hekal[d].

[a]Sanitary and Environmental Institute (SEI), Housing and Building National Research Center (HBRC), Giza, Egypt, 1770.
[b]Hydrogeochemistry Dept., Desert Research Center, El Mataryia Cairo, Egypt, 11753.
[c]Chemistry Department, Faculty of Science, Benha University, Benha, Egypt.
[d]Department of Chemistry, Faculty of Science, Ain Shams University, Abbassia, Cairo, Egypt, 11566.

Abstract

The incorporation of nanomaterials in thin film composite (TFC) has provided a new way to increase the permeability of the forward osmosis membrane during the desalination of water. In this research graphene oxide (GO), reduced graphene oxide (rGO) and carbon nanotube (MWCNT) was prepared and introduced into a polyamide layer to form TFC membrane via interfacial polymerization reaction. The properties of the membranes were characterized by using ATR- FTIR, SEM and water contact angle measurements. The obtained results illustrated that a TFC-FO membrane doped with GO (0.7wt%) has a high water flux (27.15 L $m^{-2}h^{-1}$) while membrane doped with rGO (0.5wt%) exhibits water flux (24.05 L $m^{-2}h^{-1}$), and the membrane doped with MWCNT (0.5wt%) has water flux (21.67 L $m^{-2}h^{-1}$) compared with pure membrane with water flux of (10.24 L $m^{-2}h^{-1}$).

1. Introduction

The water shortage crisis has been increased in several regions all over the world by climate change, and growing industrial and agricultural request for water. In such areas of deficiency, desalination is frequently the only solution [1]. In the present time, the membrane-based separation techniques are currently being utilized in various ways to supply fresh water from saline and contaminated water by reverse osmosis (RO), nanofiltration (NF) and forward osmosis (FO) manner. [2,3]. Lately, developing FO technology has drawn intensifying attention. Forward osmosis (FO) is a membrane-based method that is operated only by the dissimilarity in osmotic pressure across the membrane[4]. Regardless of lower water flux, comparing with RO which uses a high-pressure pump at the feed border [3], FO promotes less fouling and higher recovery[5,6]. Therefore, FO has great

potential to be used in numerous industries for example power generation, water desalination, liquid food concentration, wastewater treatment, and pharmaceutical applications[7,8]. Nevertheless, it is still facing many serious challenges that need to be overcome. Those include concentration polarization, reverse solute diffusion and the requirement for developing the membrane and the outline of the draw solute[9,10]. The most widely used membranes in the FO process are thin-film composite membranes (TFC) structured using interfacial polymerisation (IP) [11]. But, the low hydrophilicity and permeability, in addition to the high fouling propensity of the established TFC membranes blemished their uses on a large scale [12]. Thus, the key research segment in the field of membrane science is the design of a thin film composite membrane with great water permeability [13,14]. The incorporation of nanoparticles inside the rejection layer of polyamide (PA) is a modern method to improve the separation

functioning of the fabricated membranes that have been classically identified as thin film nanocomposite (TFN) membranes [15]. It has been established that the surface wettability and roughness of the TFN membranes has been greatly enhanced by the incorporation of suitable nano particles into the PA layer such as zinc oxide[16], cellulose nanocrystals[17], titanium dioxide[18], and Ferric oxide[19]. Nonetheless, the poor interactions and compatibility between the application of nanomaterials and the polymer matrix are considered to be the key challenges for the TFN membranes improvement. Adherence, interfacial interactions and consistency between the nanofiller and the polymer matrix contribute to the control of membrane durability and efficiency [15]. Nanomaterial surface modification with appropriate functional groups is one of the approaches used to resolve the aforementioned problems. Moreover, the TFN membrane made of these nanomaterials can provide better surface water permeability and hydrophilicity compared with the traditional nanomaterials without surface modification. The use of carbon nanotubes (CNTs) as nanomaterials integrating in the polymeric thin-film matrix has gained tremendous concentration because they show great potential to advance both the membrane's permeability and antifouling capability. The development of permeability of CNT embedded membranes may be due to the additional water channels produced by CNTs and the nano passages between CNTs and polymers, it may also break down the cell membranes of microorganisms and disturb the metabolic pathways accompanied by oxidative stress, and microorganisms may then be inactivated[20]. Due to their ideal material properties and dispersibility of polymer matrices, graphene derivatives (GO, rGO, GQDs) have been recognized as active fillers in polymer nanocomposite materials [21]. Above all, graphene oxide (GO) nanosheets (containing different oxygenated functional groups) exhibit great potential for creating nanocomposite materials with high chemical stability and strong hydrophilicity[22]. In the other approach, GO nanosheet was found to be a good candidate for manufacturing mixed-matrix membranes to combine the processibility of polymers and the characteristics of GO materials, it entrenched thin-film polyamide membranes have been studied for nanofiltration, reverse osmosis, treatment of oily water using hollow fiber ultrafiltration and FO applications, which showed high-flux and antifouling properties. In this study, MWCNT, GO and r GO nanosheets were incorporated into ultra-thin-film polyamide by interfacial polymerization process to form the PSF support layer. The structure and efficiency of the thin-film nanocomposite (TFN) membrane in the FO process were analyzed in terms of water flux, and the

results were compared with each other and with a thin-film composite (TFC).

2. Experimental
2.1. Chemicals and reagents

Graphite (99.995%) was purchased from Fluka Switzerland, hydrazine monohydrate (NH_2-NH_2.H_2O) 99%, and N,N' dimethylformamide (DMF) were purchased from SDFCL India, potassium permanganate ($KMnO_4$) 97%, sodium nitrate ($NaNO_3$) 95%, hydrogen peroxide (H_2O_2) 30%, ethanol (C_2H_5OH) 99%, sodium sulphate (Na_2SO_4) 98% and sulfuric acid (H_2SO_4) (98%) were purchased from Adwic pharmaceutical and chemicals company Egypt, Polysulfone Udel P-3500 in pellet form (Solvay Advanced Polymers),hexane(advent,>99%, hplc grade) and polyvinylpyrrolidone (PVP K30,Sigma-Aldrich), 1,3-phenylenediamine (MPD, >99%, Merck) and 1,3,5-benzenetricarbonyl trichloride (TMC, >98%, Merck) were used for producing membrane substrate. All the chemicals were of analytical grade, commercially available and used without further purification.

2.2. Experimental Methods
2.2.1. Preparation of Graphene oxide GO

Graphene oxide (GO) was prepared from natural graphite according to a modification of the Hummers–Offeman method [23]. In short, graphite powder (5 gm) was dispersed in concentrated sulfuric acid (H_2SO_4, 115 ml, 98 wt%, in a dry ice bath). Then, 2.5 gm $NaNO_3$ was inserted into the solution and finally 15 g potassium permanganate was little by little added with continuous vigorous stirring for 2 h at 10°C, followed by 1h at 35°C. Then, the 250 ml of deionized (DI) water was added to the mixture present in the ice bath. Once the effervescence stopped, the temperature of the mixture was increased to 98°C and held for 10 min before cooling to room temperature. Next, 50 ml of H_2O_2 was gradually added to the mixture and heated at 90°C for 30 min. The produced mixture was centrifuged and washed with boiling water until the pH of the supernatant became neutral. Finally, the obtained solid was dried at 60°C for 24 h.

2.2.2. Reduction of Graphene oxide (r GO)

Using the modified Hummer process, 0.1 g of GO obtained was first dispersed in 30 ml distilled water and sonicated for 30 minutes. With the addition of 3 ml hydrazine hydrate, the obtained suspension was then heated to 100 °C and held at this temperature for 24 h. The formed reduced graphene oxide (rGO) was collected by filtration and washed several times by distillation, accompanied by sonication to eliminate the hydrazine excess. The final product was gathered through vacuum filtration and dried at 80 °C [24].

2.2.3. Preparation of Multiwall Carbon Nanotube (MWCNT)
2.2.3.1 Preparation of the Catalysts

Impregnation and co-impregnation methods prepared the monometallic and bimetallic catalysts that contain different quantities of Co, Cr, Mo, and W supported on MgO. The required amounts of metal precursors were dissolved in deionized water for the various catalysts and then added to the MgO support. The mixtures were then evaporated under constant stirring at 80 ° C and the resulting pastes were dried at 120 °C overnight, then ground into fine powders and calcinated for 4 hours in air at 600 °C [25].

2.2.3.2 Preparation of Multiwall Carbon Nanotubes (MWCNT)

A multiwall carbon nanotube (MWCNT) was produced using the catalytic chemical vapor deposition process (CCVD) proceeding in a horizontal quartz-fixed bed flow reactor. Approximately 0.5 gm of the fresh calcined catalyst was distributed in the center of the reactor and heated to 700 ºC under a mixture of 50 cm^3/min H_2 (99.9%) and 150 cm^3/min N_2 (99.999%) with holding the catalyst at this temperature for 1 hour. After that the H_2 gas was converted for 1 hour to a mixture of 50 cm^3/min of acetylene (99.995 percent) and 150 cm^3/min of nitrogen. Lastly, the reactor was cooled to room temperature under a nitrogen flow of cm^3/min [25].

2.2.4. Preparation of polysulfone (PSF) support membrane

PSF substrates were synthesized using the phase inversion technique. The casting solution was prepared by dissolving (0.5% wt) Polyvinyl pyrrolidone (PVP) in N, N-dimethylformamide under vigorous stirring for 15 minutes at 80°C (500 rpm). Then, (15.5% wt) Polysulfone (PSF) pellets were then gently added to the solution under stirring (650 rpm) until the complete solvation of all Polysulfone pellets followed by degassing for 12 h at ambient temperature. The polyester non-woven fabric with a thickness of around 100 μm is linked with a clean glass plate followed by doping the solution on the polyester non-woven fabric using QTC Automatic film applicator with a thickness of 50μm. To facilitate phase separation, the glass plate was smoothly immersed in a precipitation bath containing DI water. The substrate was washed and deposited in deionized water for removal of the residual materials after 10 min. Then, the substrate was dried between two sheets of filter paper before being used in the next step.

2.2.5 Preparation of Thin Film Composite Membrane

The polyamide rejection layer was shaped on the pre-cast PSF substrate by the interfacial polymerization process. To initiate the process, the PSF substrate was immersed in a solution containing 2 wt% MPD, 0.15 wt% SLS in de-ionized water for 2 min. The extra MPD solution was dried by a rubber roller. Subsequently, the substrate was dribbling in a 0.53 wt % of TMC dissolved in n-hexane for 1 min. For post-treatment, the TFC membrane was put in 80°C oven for 10 min. Lastly, the organized TFC membrane was washed and kept in DI water. (GO, rGO & MWCNT)-polyamide TFN membranes were prepared by the same method, except that nanomaterials were added from the 0.53 wt/v% TMC in n-hexane solution. Different amounts of nanomaterials (0.3, 0.5, 0.7 and 0.9 wt %) were dispersed in TMC-n-hexane solution by ultrasonic for 1 h. The obtained solution was immediately used for interfacial polymerization with MPD-soaked PSF supports to form the TFN membranes.

2.3. Characterization

Nanomaterials and Membranes (GO, rGO & MWCNT) were characterized by XRD The crystalline structure and phases for all the prepared samples were analyzed as a powder by x-ray diffraction (XRD) with a Philips X'Pert Pro Super diffractometer operating in transmission mode with Cu Kα radiation (λ= 0.15418 nm) in the diffraction angle of 2θ from 5° to 80° at a scan rate of 5° min−1. The samples were measured at room temperature. Raman spectra were measured with a U-1000 laser Raman spectrometer using the 514.5 nm line of an ArC laser as the excitation beam. TEM micrographs were done using an FEI; model Tecnai G20, Super twin, double tilt 1010, at a power of 200 kV. Attenuated total reflectance Fourier transform infrared spectroscopy (ATR-FTIR) of samples was obtained with an infrared spectrometer (JASCO Fourier transform infrared spectroscopy (FT-IR) 6100 made in Japan.) at room temperature to identify the presence of nanocarbon materials in the polyamide layer. The surface morphology of the membranes was investigated with an SEM Model Quanta FEG250 SEM (FEI Company) with accelerating voltage 30 kV. Surface morphology and roughness of the membrane were characterized by atomic force microscopy (flex axiom nanosurf C3000- Static mode). AFM was done in the contact mode and the scan size was 2.5 μm × 2.5 μm. The average value of roughness measurements in three locations of the membrane surface is reported. The surface hydrophilicity of the membranes was decided by the measurement of the water contact angle with a contact angle goniometer from (VCA Video Contact Angle System, KrÜss DSA25B, Germany) using six measurements at different sites for every membrane.

_____

2.1. Measurement of membrane intrinsic separation properties

A cross-flow RO filtration device (Sterlitech Corporation) with an active membrane area of 42 cm^2 was used to evaluate pure water permeability and salt rejection efficiency of prepared membranes. Membrane pure water flux (Jw) was measured at 4 bar. In order to eliminate the effect of membrane compaction, the membranes were pressurized with DI water at 4 bar for 1 h, then the membranes were tested in cross-flow membrane permeation tests at 4 bar with a cross-flow rate of 2.5 L min^{-1} (0.32 m s^{-1}) to reduce concentration polarization. The Pure water permeability (A) (L/m^2.hr bar) was calculated according to equation 1 and 2 [26] where; $J_w{}^{RO}$ is the pure water flux based on RO (L/m^2.hr), ΔV is the permeate volume (L), A_m is the membrane active surface area (m^2), Δt is the time (hr) and P is the membrane applied pressure (bar).

$$J_W{}^{RO} = ΔV/A_m. Δt \qquad (1)$$
$$A = J_W{}^{RO} / ΔP \qquad (2)$$

The salt permeability has been studied based on the principle of solution – diffusion. Sampling was conducted at 25 °C and P = 4 bar for 1 hr after the system was stabilized. 2 g/ L of the NaCl solution was used as a feed solution for the rejection experiment. Measurement of salt concentrations using a conductivity meter. The salt rejection (R^{RO}) was determined according to equation (3)[26] where; C_F and C_P represent the concentration of feed and permeate (product) (ppm), respectively. The salt permeability coefficient (B) (L/m^2.hr) which is the intrinsic property of a membrane to retain salt, was computed using equation (4)[26] where Δπ is the osmotic pressure difference across the membrane.

$$R^{RO} = [1-(C_p / C_f)] \qquad (3)$$
$$B = A. ΔP (1/R - 1) \qquad (4)$$

2.2. Evaluation of FO Performance

The laboratory FO set-up was employed to investigate membrane implementation. The membrane was placed in a module with a membrane area of 42 cm^2 (CF042A-FO). One of the fluxes was filled with 1 M NaCl as a draw solution and the other one was filled with an equal volume of deionized water as a feed solution. Both solutions were mixed completely by the rotation of the solutions using a pump with a flow rate of 1.6 L/h. The temperatures of the feed and draw solutions have held at 23 ° C ±2 due to intense mixing. The membranes were tested in the FO mode (where the active layer in front of the feed solution or AL-FS) and the osmosis retarded pressure (PRO) mode (i.e. the active layer facing the draw solution or AL-DS). The external concentration polarization phenomenon was expected to be negligible. The volume change in draw solution was determined by Digital Weight Balance for calculation of water flux. To evaluate the FO water flux (J_W), the volume of water transferred from the feed solution to the draw solution (ΔV) was measured and applied in the equation (5)[27].

$$J_w = [V_w/ (A× Δ_t)] \qquad (L/m^2. h) \qquad (5)$$

Where V_w is the pure water volume passed through a membrane area of A within a purification time of t.

The reverse salt flux (J_s) was determined by the equation (6)[27].

$$J_s = (V_t C_t – V_o C_o)/ Δt. A \qquad (g /m^2. h) \qquad (6)$$

Where V_o and V_t are feed solution's beginning and ending volumes and C_o and C_t are feed solution's beginning and ending salt concentrations. The tests were performed at room temperature (23 ± 2 °C).

The salt rejection, R^{FO}, in FO was defined by the equation (7)[28].

$$R^{FO} = 1-(J_S / J_W)/ (C_{d\,0}+C_{d\,e})/2 *100 \qquad (7)$$

Where J_s (gm^{-2} h^{-1}) is reverse solute flux, J_w (Lm^{-2} h^{-1}) is water flux in FO, and $C_{d\,0}$, $C_{d\,e}$ are the initial and final concentration of draw solution (gm /L) respectively.

3. Results and Discussion

3.1. Characterization of Nano Materials

The XRD patterns of GO, rGO, and MWCNTs were shown in Fig. 1, the typical graphite (002) plane reflection found at 2° ~ 26.1^o shows the presence of carbon in graphite arrangement. The XRD pattern of CNTs shows two peaks at 25.9° which indicate that The prepared carbon tubes have little aggregation and are easy to separate and oxidize and 44.1° corresponding to the (0 0 2) and (1 1 0) of MWCNTs [29], The XRD pattern of GO sheets shows the prominent crystal plane (001) which approved the random packing of graphene sheets in the GO and this peak disappears in the XRD pattern of rGO. On the other hand, XRD of rGO exhibits a new broad peak at 2Θ ~25.8° corresponding to (0 0 2) plane[30].

Raman spectroscopy is an important technique for the characterization of carbon products, particularly respecting the point that conjugated and doubles carbon-carbon bonds direct to high Raman intensities in Fig. 2. The specific Raman bands and their intensity ratios give valuable knowledge about the graphene structure such as D/G band intensity ratio, which signifies defects, while 2D/G denotes the number of layers in graphene[31]. The D vibration band which can be seen at 1343, 1340 and 1327cm^{-1} for GO, rGO and MWCNT respectively is attributed to the existence of disorder in carbon systems and was the consequence of structural imperfection by the attachment of oxygen functionalities to the basal plane of carbon. On the other hand, the G vibration band for sp^2 carbon appeared at 1578 for GO, 1588 for rGO and 1573 cm^{-1} for MWCNT. Moreover, the G vibration band also supplied a stretching C-C bond,

_____

which is public in all carbon sp^2 systems [32]. The 2D peak observed at 2769 for GO, 2700 for rGO and 2681 cm^{-1}for MWCNT is due to double resonance transitions causing the production of two photons with opposite momentum. Contrasting to the D peak, which is Raman active only in the existence of defects, the 2D peak is active even in the absence of any defects. Accordingly, the position of the 2D band thus verifies that the resulting GO was multilayer, as the monolayer graphene usually observed at 2679 cm^{-1} in the Raman spectrum. Moreover, the shift occurring at the 2D band location is due to the presence of functional groups containing oxygen which prevent the stack graphene layer. The Raman spectrum of rGO presented in Fig. 2 also shows the 2D band at 2700 cm^{-1}. This is because, after GO was reduced to rGO, fewer residue

of functional groups containing oxygen remained and caused the rGO to stack [33].

The FTIR spectrum of MWCNT, GO and r GO are shown in Fig. 3. GO shows a broad peak in the range of 3000 - 3500 cm^{-1} corresponding to the stretching vibration of OH groups of water molecules adsorbed on GO [34], besides –C=O stretching (–COOH group) band at 1739 cm^{-1}. The peaks observed at 1560 and 1648 cm^{-1} are assigned to the aromatic C=C group in the GO sample [35], whereas the epoxy group (C-O-C stretching) is observed at a wavelength of 1339 and 1117 cm^{-1}. All the detected oxygenated groups confirmed that GO was synthesized successfully[36]. FTIR spectrum of the reduced graphene oxide (rGO) sample shows the oxygenated functional group with broad O-H stretching vibration and C-O stretching vibration at 3445 cm^{-1} and 1394 cm^{-1}, respectively. It is also notable that other peaks at 1741, 1135 and 1015 cm^{-1} confirmed oxygen removal during the reduction process by using hydrazine hydrate. This means that the functional groups containing oxygen have been largely removed effectively and the minimal quantities of the residue of functional groups remain on the edge and basal plane of r GO. The FT-IR spectrum of MWCNT shows peaks at 1645, 1540 and 3430 cm^{-1} attributed to the stretching vibration groups of C=O, -C-O-C, and OH-, respectively.

Fig. 4 show the SEM micrographs of the investigated samples. The GO SEM micrograph shows wrinkled and layered flakes on the surface. The presence of flakes means that the layers of graphene were completely oxidized to GO [37]. In addition, the rGO micrograph shows that the rGO surface contained crumpled thin sheets that accumulated to form a disordered structural material [38]. Whereas the micrograph of MWCNT shows a

worm structure with diameters ranging between 42 and 51 nm[39].

The TEM images of GO and rGO, given in Fig. 4 show a sheet-like morphology with different transparencies and thickness. Dark areas refer to a thick stacking nanostructure of several GO layers, whereas the higher transparency areas refer to much thinner films of a few GO layers. On the other hand, the TEM image of MWCNT shows a tubular structure with diameters ranged between 2 and 6 nm[40].

Fig. (1) XRD patterns of the prepared GO, rGO and MWCNT samples.
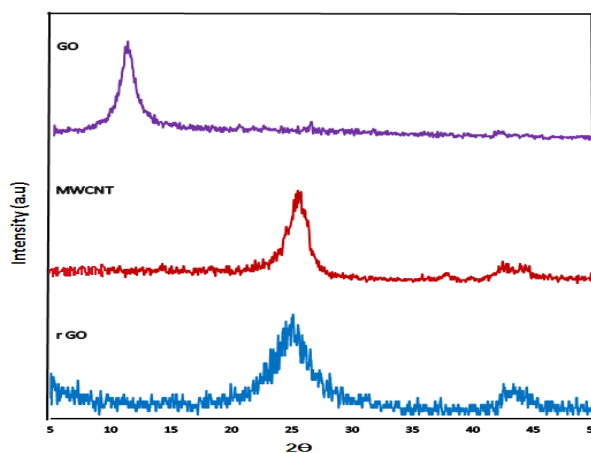
Fig. (2): Raman spectra of GO, rGO and MWCNT samples.
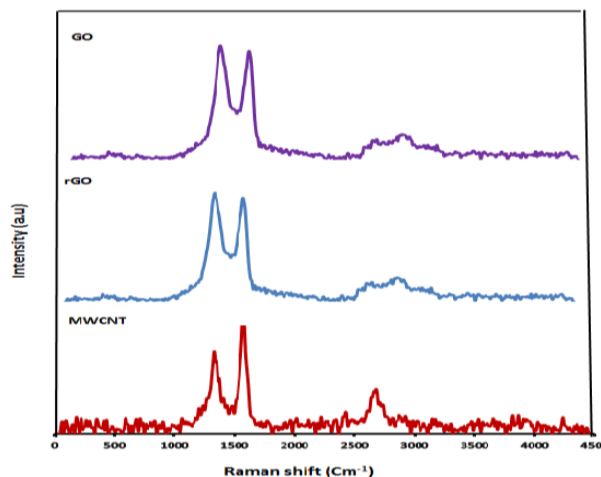
3.1 Morphology and surface properties of GO, rGO and MWCNT incorporated FO membranes

A comparison between the ATR-FTIR spectra of the thin film composite (TFC) and thin-film nanocomposite membranes (TFN) containing GO, rGO and MWCNT membranes are shown in Fig. 6. The spectra show the characterizing peaks of the PA layer at 1609 cm^{-1}, 1654 cm^{-1} and 1541 cm^{-1}, which are assigned to the aromatic ring breathing, amide II band (C=O stretching) and amide II band (C–N stretching), respectively. No observable variations were noticed concernig the intensity of the peaks between the TFC and TFN (GO, rGO and MWCNT) membranes[41.42] , as revealed in Fig. 5. The peak observed at ~ 2950 cm^{-1} is linked with C–H stretching groups and the higher intensity peak appeared at 1609 cm^{-1} might be matching to the increment of N–H groups. It was also noted that the introduction of (GO, rGO and MWCNT) causes in some cases a change in the intensity of the peaks, whereas the incorporation of (GO, rGO and MWCNT) may influence the formation of amide bonds. The appearance of a peak at 1728 cm^{-1} in the spectrum of TFN GO 0.7 corresponds to the carbonyl (C=O) of GO which is present as a large amount in the sample[43].

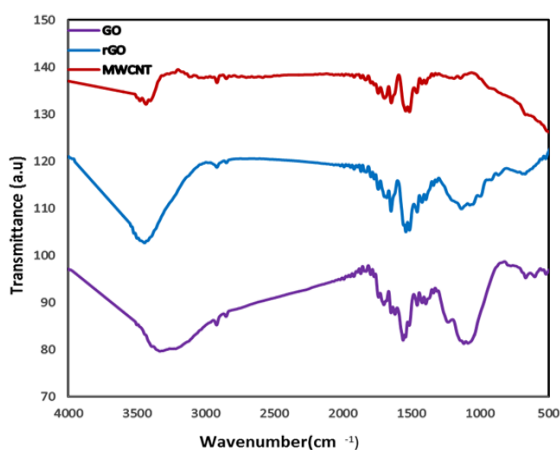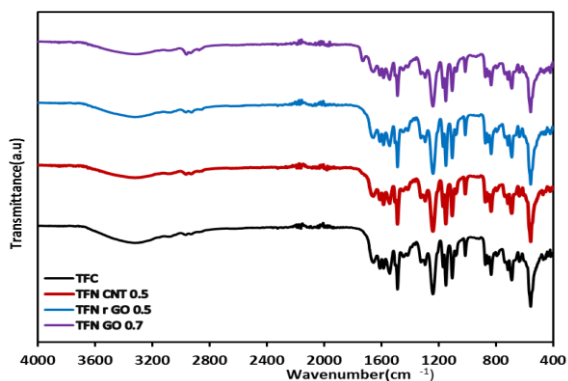**Fig. 3: FTIR spectrum of GO, rGO and MWCNT Samples.**

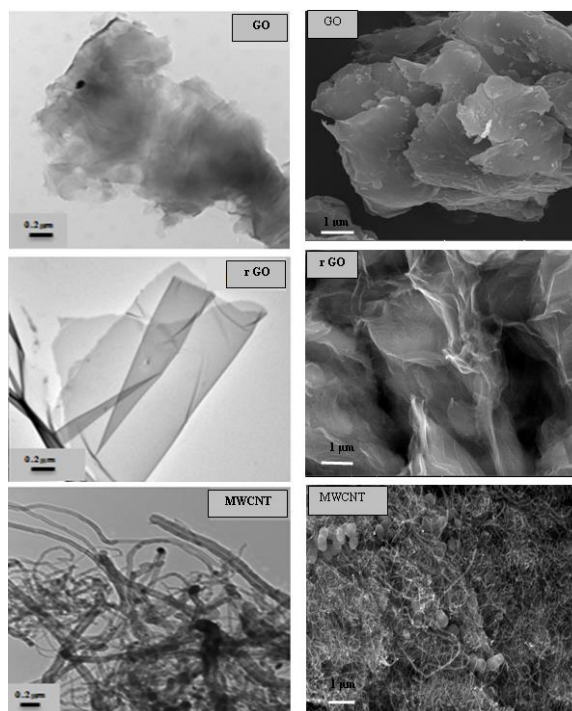**Fig. 5: TEM & SEM of GO, rGO and MWCNT.**

Fig. 4: ATR FTIR of TFC and TFN-GO 0.7, TFN-rGO 0.5 and TFN-MWCNT 0.5.

The surface morphologies of the TFC and TFN membranes are given in the top-view SEM images of the membrane with different nanocarbon structures stuffing in Fig. 6. Both the TFC and TFN membranes indicated a ridge-valley-like structure on their surfaces, which is a feature of the polyamide (PA) membrane due to interfacial polymerization process. Detailed observation shows that TFC membrane presented a more nodular surface relative to denser structure of TFN membranes. This shows the great changes in membrane surface morphology after addition of GO, rGO and MWCNT which are attributed to the reaction rate of interfacial polymerization. The fast reaction of MPD with TMC resulted in a nodular structure. The slow reaction of TMC and carboxyl group might lead to a denser surface. It is also attributed to the formation of hydrogen bond between hydroxyl group and the polymer chain [44].

Fig. 7 demonstrates three-dimensional TFC and TFN membrane AFM micrographs. The study of the images reveals that GO, rGO and MWCNT have strengthened both the surface pores and nodules, and that the roughness of the substratum is due to the height of the lumps on the surface [45]. The R$_{MS}$ values of TFC and TFN membranes with identical support layers proposed that the existence of GO, rGO and MWCNT causes the enhancement of surface roughness; the R$_{MS}$ value of TFN-GO 0.7 (R_{MS}=54.6 nm) is higher than that of TFC membrane (R_{MS}=15.3 nm). The surface characteristic parameters: surface average roughness (Ra), the root mean square of the Z value (R$_{MS}$) and (R$_Z$) the mean height difference between the peaks ground of the

TFC sample to the final TFN is found to be changed. These changes in the alleged parameters are listed numerically in Table 1 for better comparison.
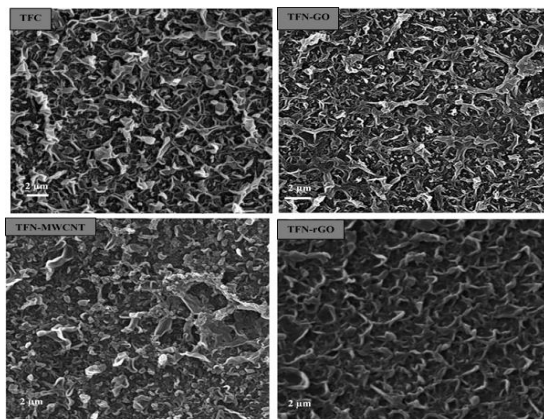

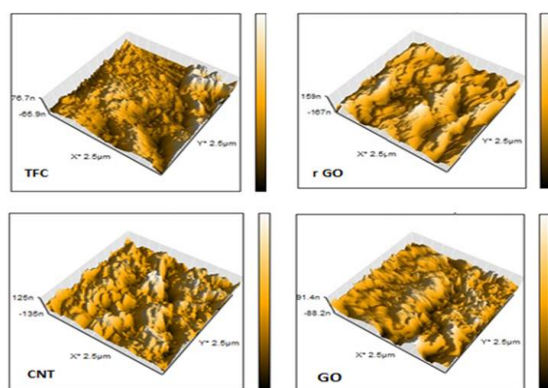**Fig. 6: SEM of TFC and TFN-GO 0.7, TFN-rGO 0.5 and TFN-MWCNT 0.5.**

Fig. 7: AFM of TFC and TFN-GO 0.7, TFN-rGO 0.5 and TFN-MWCNT 0.5.

The hydrophilicity of the investigated TFC and TFN membranes was studied using the contact angle measurement and the results obtained are given in Fig.8, and Table 1. The contact angle value shows the affinity of water to wet the membrane surface, where the lessen value refers to the higher affinity for water to wet the membrane and the better hydrophilicity. The obtained results show that the contact angle of the TFN membrane reduces by the addition of GO, rGO, and MWCNT into the membrane. The surface contact angle and hydrophilicity have an inverse correlation. Increasing the membrane surface hydrophilicity is owing to the existence of the hydrophilic functional group such as hydroxyl, carboxyl, and epoxy on GO nanosheets and morphology of CNT. Moreover, the increase in the surface roughness of the membranes by loading the nanomaterials (GO- rGO- MWCNT) into the

membrane would be another reason for the enhancement of the water contact angle.

3.2 Membrane separation properties

The separation properties of TFC and TFN membranes including water permeability (A), NaCl permeability (B), and NaCl rejection (R) were described in Table 4. Water permeability in Fig. 9 was increased with the addition of nanocarbon materials (A = 3.51, 2.62 and 2.14 L/m^2 h bar for TFN compared to 1.85 L/m^2 h bar for TFC). The improvement in hydrophilicity of membranes enhances water permeability by facilitating water molecules to pass through the membrane. The improvement would be due to the incorporation of some holes at the interface of GO, rGO and MWCNT/polyamide, although this water flux increase might be followed by more salt permeation. Increasing the surface coarseness of the polyamide layer by the addition of nanocarbon materials would be another reason for higher water permeability. All of the synthesized membrane showed greater permeability to water. The low salt permeability is representative of the membrane's high rejection power. The TFN membranes exhibited higher salt rejection compared with that of the control TFC membrane. The salt rejection improved by adding carbon nanomaterials from 89.2 % for the TFC membrane to 91.03, 93.34 and 95.7 %. The B / A ratio is an important parameter that marks the selectivity of the membrane in FO [46]. Small B/A ratio shows low solute reverse diffusion and high water permeability. Where the TFN-GO 0.7 showed the lowest B/A ratio representing the best membrane selectivity.
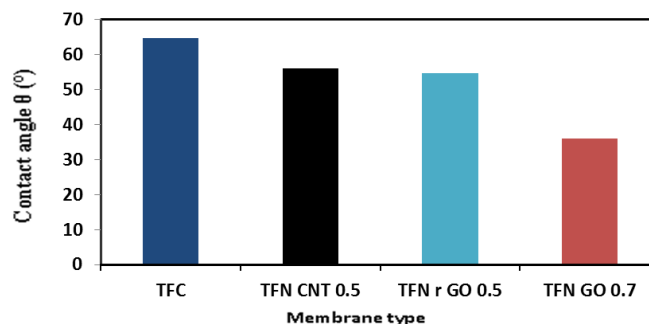
Fig. 8: Contact angle of TFC and TFN-GO 0.7, TFN-rGO 0.5 and TFN-MWCNT 0.5.

Table 1 AFM data & Contact angle measurements of synthesized TFC and TFN-FO membranes.

Membrane	R_a (nm)	R_{ms} (nm)	R_z (nm)	Contact angle θ (°)
TFC	10.58	15.34	212.07	64.8
TFN-GO 0.7	41.68	54.58	481.39	35.9
TFN-r GO 0.5	36.34	45.39	347.88	54.6
TFN-CNT 0.5	30.10	38.97	435.24	56.1

_____

3.3 FO Experiments

The FO of the TFC and TFN fabricated membranes showed the high water flux in each of AL- (active layer facing draw solution) and AL- (active layer facing feed solution) orientations where FS contained deionized water and DS enclosed 1 M NaCl. Similar to the orientation of AL-FS, AL-DS shows the higher water flux. The results obtained are shown in Fig. 10, showing a higher water flux and solute flux (rejection) of the modified membranes than that of the TFC membrane. The water flux of the TFC membrane was significantly improved from 17.58 to 40.01 L/m^2 h for TFN-GO 0.7 in AL-DS mode and from 10.24 to 27.14 L/m^2 h in FO mode. The addition of more GO nanosheets leads to a reduction in water flux. The increase in water flux with increasing GO loading from 0.3% to 0.7% is due to improving the hydrophilicity of the TFN membranes owing to the existence of hydroxyl and carboxyl groups on GO nanosheets and the increase in surface area (roughness) of the membranes. Further increase in GO loading resulted in water flux reduction. This might be due to the aggregation of GO at higher concentrations leading to the non-uniform distribution of GO in the thin-film layer[47]. The water flux of TFC membrane was also developed from 17.58 to 36.50 L/m^2 h for TFN- rGO 0.5 in AL-DS mode and from 10.24 to 24.04 L/m^2 h in FO mode, owing to the increase in both roughness and the contact angle of the polyamide/rGO membrane, which is differ from that of the polyamide membrane. This indicates that the introduction of rGO into the membrane develops the hydrophilicity due to incomplete reduction of GO which some groups of hydroxyl and carboxyl groups still on the surface of reduced graphene and the charge of the membrane surface, which is useful for increasing the permeation flux. But for a concentration of rGO more than 0.5 wt%, the water flux is found decreased in both modes due to when graphene oxide reduced by hydrazine to obtain reduced graphene the deformations on the surface have been incompletely treated and have become very similar to the graphite, in which the carbon structure is more systematic and that works to block the pores[24]. Table 4 shows also that the water flux of the TFC membrane is enhanced from 17.58 to 35.96 L/m^2 h for TFN-MWCNT 0.5 in AL-DS mode and from 10.24 to 21.67 L/m^2 h in FO mode. The water flux formed in TFN membranes is due to the presence of MWCNTs that react in the upper surface of the membranes as nano channels. Each of the inner cores of nanotubes and the interfacial distance between the MWCNTs and polymer at the polyamide layer interface (external nano channels) provide additional ways of transporting water. The latter works as a key role because the internal nano channels are too small to extract water without applying pressure (FO mode). In addition, the external nano channels provide a clear and correct direction relative to the inner cores. The polyamide / MWNTs membrane contact angle is lessen than that of the polyamide membrane, due to the fact that the incorporation of MWNTs into the membrane increases both hydrophilicity and the membrane surface charge, which is useful for increasing the permeation flux. Nevertheless, the rise in MWCNT loading resulted in a decrease in water flow due to the increase of internal nano channels that are too thin to extract water without applying pressure[48]. When comparing these results with what was mentioned in previous studies, we find that the graphene oxide and reduced graphene give better results as shown in the table 4. Orientation is one of the important factors influencing FO efficiency, Water flux is lower than DS mode due to the more intense ICP in FO mode [49]. On a practical point of view this is of great importance to FO application.

Solute flux through membranes is presented in Fig. 11. The reverse salt fluxes in TFN-GO 0.7 (1.08 for AL-FO and 7.61 for AL-DS), TFN-rGO 0.5(2.28 for AL-FO and 8.33 for AL-DS) and TFN-MWCNT 0.5(2.99 for AL-FO and 11.84 for AL-DS) membranes are all lower than TFC(6.53 for AL-FO and 14.11 for AL-DS) membrane, moreover, by increasing the GO, rGO nanosheets and MWCNT loading, the solute flux decreased to reach a minimum at 0.5 wt.% for MWCNT and rGO as well as at 0.7 wt.% for GO, before starting to increase again. The higher solute flux at the higher loading concentrations of the Nanomaterials may be attributed to the agglomeration of nanostructure on the film surface which limits the arrangement of the perfect thin film of polyamide layer. According to the water and solute fluxes, the loading of 0.7 wt. % is selected as the optimum content of the GO in the active layer of the GO- nanocomposite membrane and 0.5 wt.% is selected as the optimum content of the rGO and MWCNT in active layers of the rGO-nanocomposite and MWCNT-composite membranes. The ratio of water flux to reverse salt flux (J_S/J_W) is also reported for better comparison, and is presented in in Fig. 12. Which means lower reverse diffusion of NaCl in our work[50]. This study showed a serious demand to optimize graphene oxide, reduced graphene, and multiwall carbon nanotube processing, as overloading of these materials may not be beneficial for FO efficiency and may even have a negative impact on the properties of the FO membranes.
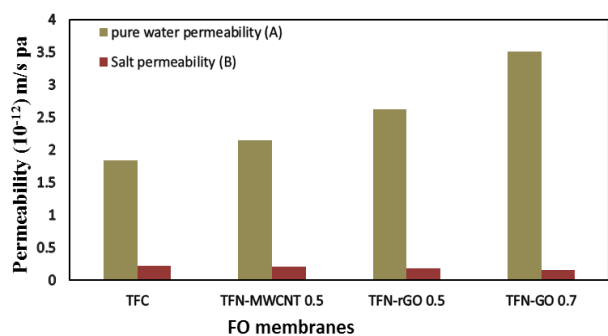
_____

Fig. 9: Water permeability and salt permeability of synthesized FO membranes.
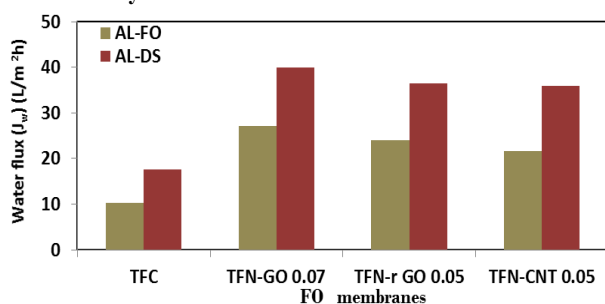

Fig. 10: Pure water flux of TFC membranes tested in both AL-FO and AL-DS modes. (Feed solution: DI water, draw solution: 1 M NaCl).
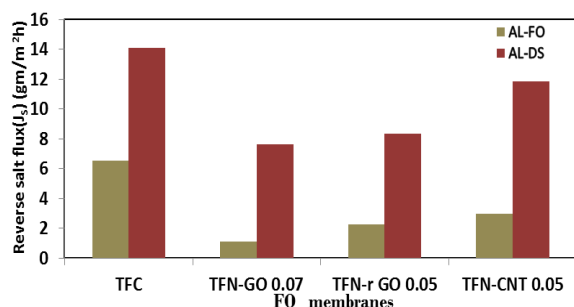

Fig. 11: Reverse salt flux of TFC membranes in both AL-FO and AL-DS modes. (Feed solution: DI water, draw solution: 1 M NaCl).
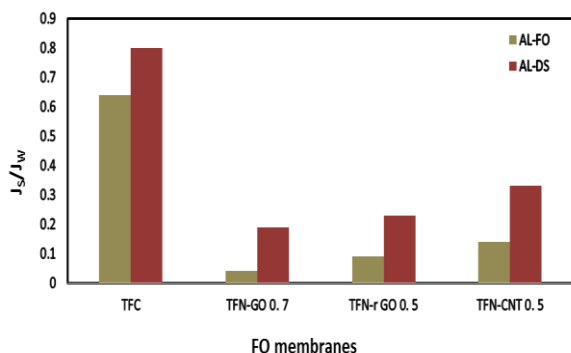

Fig. 12: Specific reverse flux selectivity of TFC membranes in both AL-FO and AL-DS modes. (Feed solution: DI water, draw solution: 1 M NaCl).
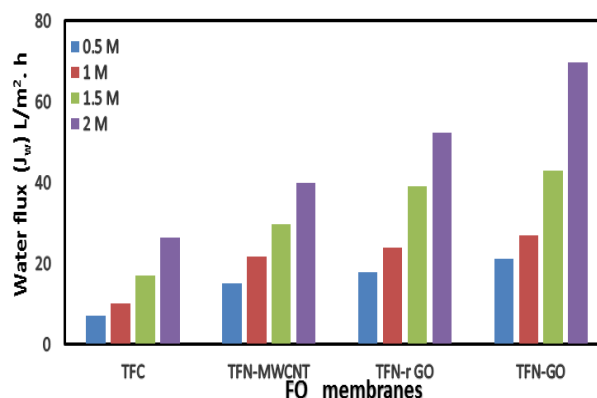

Fig. 13: Water flux at different NaCl draw concentrations.

3.4 Effects of NaCl Draw Solution Concentration on FO performance

The water flux for TFC and TFN-GO 0.7, TFN-rGO 0.5 and TFN-MWCNT 0.5 at different DS concentrations (0.5, 1, 1.5, and 2 M NaCl) is illustrated in Fig. 13. It indicates that the water flux increases as the concentration of the draw (NaCl) solution increases from 0.5 M to 2 M, which can be interpreted based on the osmotic pressure increase which is the driving force in FO. In addition, it is important to note that the rise in water flux by the membrane of TFN-GO 0.7, TFN-rGO 0.5 and TFN-MWCNT 0.5 is significantly higher than that of the TFC membrane.

Table 2: Separation properties of synthesized TFC and TFN-FO membranes.

FO membrane	[a]Pure water permeability A [L/(m² h bar)]	Salt rejection R (%)	[b]Salt permeability, B (L/m² h)	B/A
TFC	1.85	89.2	0.22	0.12
TFN-GO 0.7	3.51	95.7	0.16	0.04
TFN-r GO 0.5	2.62	93.34	0.19	0.07
TFN-CNT 0.5	2.14	91.03	0.21	0.09

[a] DI water is used as the feed solution in the RO test with an applied pressure of 4 bar (2.5L/min).

[b] 2000 ppm NaCl solution is used as the feed solution in the RO test with an applied pressure of 4 bar (2.5 L/min).

Table 3 Comparison between the performance of the FO membranes prepared in this work and FO membranes reported in the literature in FO/PRO modes.

| FO membrane | Water flux (Jw) (L/m² h) | | Reverse salt flux (Js) (g/m² h) | | Js/Jw (g/L) | | R^{FO} | FS | DS (M NaCl) | Ref. |
	AL-FO	AL-DS	AL-FO	AL-DS	AL-FO	AL-DS				
TFC	10.24	17.58	6.53	14.11	0.64	0.8	98.91	DI	1 M	This work
TFN-GO 0. 7	27.14	40.01	1.08	7.61	0.04	0.19	99.93	DI	1 M	This work
TFN-r GO 0. 5	24.04	36.5	2.28	8.33	0.09	0.23	99.83	DI	1 M	This work
TFN-CNT 0. 5	21.67	35.96	2.99	11.84	0.14	0.33	99.76	DI	1 M	This work
PA-GO	14.5	34.7	2.6	4.7	0.17	0.13	----	DI	1 M	[27]
PA-TiO₂	17.1	30.2	2.9	6.66	-----	-----	-----	10 mM NaCl	0.5 M	[51]
PA-TiO₂	29.7	56.7	7.3	14.4	-----	------	-----	10 mM NaCl	2 M	[51]
PA-FMWCNT	40	95	3	5.5	------	------	------	10 mM NaCl	2M	[44]
PA- GQDs	12.9	----	1.41	-----	0.11	-----	-----	DI	0.5M MgCl₂	[50]
PA- CaCO3	25.4	43.0	-----	-----	-----	-----	------	DI	2M	[28]

4. Conclusion

In the presence of nanocarbon structures in n.hexan layer, new thin-film nanocomposite (TFN) membranes were prepared by interfacial polymerisation of MPD and TMC on the PSF support membrane and equated with the TFC-FO membrane. The membranes including nanocarbon structures displayed high FO efficiency. The analyses of the AFM images and contact angle data showed an increase in each of the roughness and hydrophilicity of the TFN membranes. The water flux and reverse solute flux of the membranes were enhanced with the presence of nanocarbon structures. The TFC-FO membrane doped with GO (0.7wt %) has a high water flux (27.15 L m^{-2}h^{-1}) while membrane doped with rGO (0.5wt %) exhibits water flux (24.05 L m^{-2}h^{-1}), membrane doped with MWCNT (0.5wt %) has water flux (21.67 L m^{-2}h^{-1}) compared with pure membrane

with water flux of (10.24 L m^{-2}h^{-1}). This study indicates that the thin-film composite membrane modified by GO could be used as a promising technique for enhancing forward osmosis water flux.

5. Conflicts of interest

The authors declare that they have no known competing financial interests or personal relationships that could have appeared to influence the work reported in this paper.

6. Acknowledgment

7. References

1. Jury, W.A. and H. Vaux, *The role of science in solving the world's emerging water problems.* Proceedings of the National Academy of Sciences, 2005. **102**(44): p. 15715-15720.

2. Esfahani, M.R., et al., *Nanocomposite membranes for water separation and purification: Fabrication, modification, and applications.* Separation and Purification Technology, 2019. **213**: p. 465-499.

3. Lee, S., et al., *Comparison of fouling behavior in forward osmosis (FO) and reverse osmosis (RO).* Journal of Membrane Science, 2010. **365**(1-2): p. 34-39.

4. Widjojo, N., et al., *The role of sulphonated polymer and macrovoid-free structure in the support layer for thin-film composite (TFC) forward osmosis (FO) membranes.* Journal of Membrane Science, 2011. **383**(1-2): p. 214-223.

5. McGovern, R.K., *On the potential of forward osmosis to energetically outperform reverse osmosis desalination.* Journal of Membrane Science, 2014. **469**: p. 245-250.

6. Zhao, S., et al., *Recent developments in forward osmosis: opportunities and challenges.* Journal of membrane science, 2012. **396**: p. 1-21.

7. Nguyen, N.C., et al., *Application of forward osmosis on dewatering of high nutrient sludge.* Bioresource technology, 2013. **132**: p. 224-229.

8. Chung, T.-S., et al., *Emerging forward osmosis (FO) technologies and challenges ahead for clean water and clean energy applications.* Current Opinion in Chemical Engineering, 2012. **1**(3): p. 246-257.

9. McCutcheon, J.R. and M. Elimelech, *Influence of concentrative and dilutive internal concentration polarization on flux behavior in forward osmosis.* Journal of membrane science, 2006. **284**(1-2): p. 237-247.

10. Gray, G.T., J.R. McCutcheon, and M. Elimelech, *Internal concentration polarization in forward osmosis: role of membrane orientation.* Desalination, 2006. **197**(1-3): p. 1-8.

11. Shen, L., J. Zuo, and Y. Wang, *Tris (2-aminoethyl) amine in-situ modified thin-film composite membranes for forward osmosis applications.* Journal of Membrane Science, 2017. **537**: p. 186-201.

12. Lin, L., et al., *Identifying facile and accurate methods to measure the thickness of the active layers of thin-film composite membranes–A comparison of seven characterization techniques.* Journal of membrane science, 2016. **498**: p. 167-179.

13. Hamid, M., et al., *Effects of surface charge of thin-film composite membrane on copper (II) ion removal by using nanofiltration and forward osmosis process.* Journal of Water Process Engineering, 2020. **33**: p. 101032.

14. Sahebi, S., et al., *Effect of sulphonated polyethersulfone substrate for thin film composite forward osmosis membrane.* Desalination, 2016. **389**: p. 129-136.

15. Lau, W., et al., *A review on polyamide thin film nanocomposite (TFN) membranes: History, applications, challenges and approaches.* Water research, 2015. **80**: p. 306-324.

16. Pal, A., et al., *Nano-ZnO impregnated inorganic–polymer hybrid thinfilm nanocomposite nanofiltration membranes: an investigation of variation in structure, morphology and transport properties.* RSC Advances, 2015. **5**(43): p. 34134-34151.

17. Asempour, F., et al., *Synthesis and characterization of novel Cellulose Nanocrystals-based Thin Film Nanocomposite membranes for reverse osmosis applications.* Desalination, 2018. **439**: p. 179-187.

18. Emadzadeh, D., et al., *Synthesis, modification and optimization of titanate nanotubes-polyamide thin film nanocomposite (TFN) membrane for forward osmosis (FO) application.* Chemical Engineering Journal, 2015. **281**: p. 243-251.

19. Lakhotia, S.R., M. Mukhopadhyay, and P. Kumari, *Iron oxide (FeO) nanoparticles embedded thin-film nanocomposite nanofiltration (NF) membrane for water treatment.* Separation and Purification Technology, 2019. **211**: p. 98-107.

20. Azelee, I.W., et al., *Enhanced desalination of polyamide thin film nanocomposite incorporated with acid treated multiwalled carbon nanotube-titania nanotube hybrid.* Desalination, 2017. **409**: p. 163-170.

21. Smith, A.T., et al., *Synthesis, properties, and applications of graphene oxide/reduced graphene oxide and their nanocomposites.* Nano Materials Science, 2019. **1**(1): p. 31-47.

22. Peng, W., et al., *A review on heavy metal ions adsorption from water by graphene oxide and its composites.* Journal of Molecular Liquids, 2017. **230**: p. 496-504.

23. Alam, S.N., N. Sharma, and L. Kumar, *Synthesis of graphene oxide (GO) by modified hummers method and its thermal reduction to obtain reduced graphene oxide (rGO).* Graphene, 2017. **6**(01): p. 1-18.

24. Sharma, N., et al. *Synthesis and characterization of graphene oxide (GO) and reduced graphene oxide (rGO) for gas sensing application.* in *Macromolecular Symposia.* 2017. Wiley Online Library.

25. Awadallah, A.E., et al., *Correlation between periodicity and catalytic growth activity of bimetallic Co-group VI/MgO catalysts for production of carbon nanotubes by acetylene using chemical vapor deposition.* Fullerenes, Nanotubes and Carbon Nanostructures, 2015. **23**(7): p. 591-598.

26. Ghanbari, M., et al., *Minimizing structural parameter of thin film composite forward osmosis membranes using polysulfone/halloysite nanotubes as membrane substrates.* Desalination, 2016. **377**: p. 152-162.

27. Shokrgozar Eslah, S., et al., *Forward osmosis water desalination: Fabrication of graphene oxide-polyamide/polysulfone thin-film nanocomposite membrane with high water flux and low reverse salt diffusion.* Separation Science and Technology, 2018. **53**(3): p. 573-583.

28. Liu, Z., et al., *Investigation of internal concentration polarization reduction in forward osmosis membrane using nano-CaCO3 particles as sacrificial component.* Journal of Membrane Science, 2016. **497**: p. 485-493.

29. Das, R., et al., *Carbon nanotubes characterization by X-ray powder diffraction–A review.* Current Nanoscience, 2015. **11**(1): p. 23-35.

30. Johra, F.T., J.-W. Lee, and W.-G. Jung, *Facile and safe graphene preparation on solution based platform.* Journal of Industrial and Engineering Chemistry, 2014. **20**(5): p. 2883-2887.

31. Gupta, V., et al., *Higher oxidation level in graphene oxide.* Optik, 2017. **143**: p. 115-124.

32. Hack, R., et al., *Characterization of graphene nanosheets obtained by a modified Hummer's method.* Matéria (Rio de Janeiro), 2018. **23**(1).

33. Hidayah, N., et al. *Comparison on graphite, graphene oxide and reduced graphene oxide: Synthesis and characterization.* in *AIP Conference Proceedings.* 2017. AIP Publishing LLC.

34. Stobinski, L., et al., *Graphene oxide and reduced graphene oxide studied by the XRD, TEM and electron spectroscopy methods.* Journal of Electron Spectroscopy and Related Phenomena, 2014. **195**: p. 145-154.

35. Emiru, T.F. and D.W. Ayele, *Controlled synthesis, characterization and reduction of graphene oxide: A convenient method for large scale production.* Egyptian Journal of Basic and Applied Sciences, 2017. **4**(1): p. 74-79.

36. Strankowski, M., et al., *Polyurethane nanocomposites containing reduced graphene oxide, FTIR, Raman, and XRD studies.* Journal of Spectroscopy, 2016. **2016**.

37. Dubey, S.P., et al., *Synthesis and characterization of metal-doped reduced graphene oxide composites, and their application in removal of Escherichia coli, arsenic and 4-nitrophenol.* Journal of Industrial and Engineering Chemistry, 2015. **29**: p. 282-288.

38. Stankovich, S., et al., *Synthesis of graphene-based nanosheets via chemical reduction of exfoliated graphite oxide.* carbon, 2007. **45**(7): p. 1558-1565.

39. Zhang, J., et al. *Fabrication and experimental testing of individual multi-walled carbon nanotube (CNT) based infrared sensors.* in *SENSORS, 2007 IEEE.* 2007. IEEE.

40. Gohier, A., et al., *All-printed infrared sensor based on multiwalled carbon nanotubes.* Applied Physics Letters, 2011. **98**(6): p. 063103.

41. Shen, L., S. Xiong, and Y. Wang, *Graphene oxide incorporated thin-film composite membranes for forward osmosis applications.* Chemical Engineering Science, 2016. **143**: p. 194-205.

42. Song, X., et al., *Fabrication of carbon nanotubes incorporated double-skinned thin film nanocomposite membranes for enhanced separation performance and antifouling capability in forward osmosis process.* Desalination, 2015. **369**: p. 1-9.

43. Song, X., et al., *Nanocomposite membrane with different carbon nanotubes location for nanofiltration and forward osmosis applications.* ACS Sustainable Chemistry & Engineering, 2016. **4**(6): p. 2990-2997.

44. Amini, M., M. Jahanshahi, and A. Rahimpour, *Synthesis of novel thin film nanocomposite (TFN) forward osmosis membranes using functionalized multi-walled carbon nanotubes.* Journal of membrane science, 2013. **435**: p. 233-241.

45. Ahmed, M., et al., *Performance evaluation of a thermoresponsive polyelectrolyte draw solution in a pilot scale forward osmosis seawater desalination system.* Desalination, 2019. **452**: p. 132-140.

46. Tang, C.Y., et al., *Coupled effects of internal concentration polarization and fouling on flux behavior of forward osmosis membranes during humic acid filtration.* Journal of membrane science, 2010. **354**(1-2): p. 123-133.

47. Wu, H., B. Tang, and P. Wu, *Optimizing polyamide thin film composite membrane covalently bonded with modified mesoporous silica nanoparticles.* Journal of membrane science, 2013. **428**: p. 341-348.

48. Ma, H., et al., *Highly permeable polymer membranes containing directed channels for water purification.* 2012, ACS Publications.

49. Deshmukh, A., et al., *Desalination by forward osmosis: Identifying performance limiting parameters through module-scale modeling.* Journal of membrane science, 2015. **491**: p. 159-167.

50. Xu, S., et al., *Novel graphene quantum dots (GQDs)-incorporated thin film composite (TFC) membranes for forward osmosis (FO)*

desalination. Desalination, 2019. **451**: p. 219-230.

51. Emadzadeh, D., et al., *A novel thin film composite forward osmosis membrane prepared from PSf–TiO2 nanocomposite substrate for water desalination.* Chemical Engineering Journal, 2014. **237**: p. 70-80.

8. Abbreviations

AFM	atomic force microscopy
ATR-FTIR	attenuated total reflectance Fourier transform infrared spectroscopy
DI	Deionized
FO	forward osmosis
GO	graphene oxide
ICP	internal concentration polarization
	1,3-phenylenediamine
MPD	1,3-phenylenediamine
MWCNT	multi-walled carbon nanotube
NaCl	sodium chloride
PA	Polyamide
PSF	Polysulfone
PRO	pressure-retarded osmosis
PVP	polyvinyl pyrrolidone
rGO	Reduced graphene
SEM	scanning electron microscope
TEM	transmission electron microscope
TFC	thin-film composite
TFN	thin-film nanocomposite
TFN-GO	thin-film doped by GO
TFN-MWCNT	thin-film doped by MWCNT
TFN-r GO	thin-film doped by r GO
TMC	trimesoyl chloride